Hall Thruster Simulations with a Two-Dimensional Potential Solver and Kinetic Mobility Model

Lubos Brieda*
Particle In Cell Consulting LLC, Falls Church, VA 22046
Michael Keidar†
The George Washington University, Washington, D.C. 20052

Despite some advancements in the field, Hall thrusters are still typically simulated using quasi-1D codes that assume thermalized potential along magnetic field lines and an analytical model for the cross-field mobility. In this paper, we develop methodology and present results from a Hall thruster simulation which diverges from this approach in two important aspects. First, a two-dimensional model based on current conservation is used to compute the potential. Secondly, we utilize a kinetic model to compute mobility self-consistently. Preliminary results from this approach are demonstrated using the PPPL cylindrical Hall thruster geometry.

I. Introduction

In a recent paper [1], we reported on development of a multiscale model for self-consistent computation of cross-field mobility in Hall thrusters. The formulation is based on the observation that since electrons are magnetized, their motion along each field line can be considered independently. As such, it is possible to define a "lambda" mesh spanning the thruster channel, with each radial grid line corresponding to a selected magnetic field line. Knowing heavy particle densities, electron temperature, and the cross-field component of electric filed allows us to perform kinetic simulation of electron transport about the magnetic field line. Unlike in the case of a fully-kinetic Hall thruster code, this approach requires electron modeling for only a small subset of the device: namely several magnetic field lines. Initial results from this approach were presented in the previous work and are expanded upon in this work. The electron transport simulations were performed with a Particle In Cell (PIC) code Lynx. Heavy particle collisions and wall interactions, including production of secondary electrons, were taken into account. This detailed wall treatment allows us to investigate near wall conductivity [2], which is theorized to be a possible contributor to the so-called anomalous diffusion. Mobility is computed from guiding center drift speed. The result is a self-consistently determined mobility evaluated at grid nodes of the lambda mesh.

In the previous work, we used HPHall [3] to obtain inputs for the kinetic simulation. HPHall was run with an analytical mobility model for several tens of thousands of time steps. The results were saved to a file which was read in by Lynx. Through this process, we identified two issues forcing us to move away from HPHall. First, since Lynx and HPHall were written in different programming languages (Java and C, respectively), it was difficult to integrate them directly. The approach of writing intermediate data to a disk was not a viable long-term solution, as it was not amenable to an automated coupling of the two codes. Secondly, since HPHall implements the thermalized potential model, electron currents are volume-averaged over each field line. It was not clear if this quasi-1D approach would allow us to resolve enough near-wall physics, or be applicable to advanced thruster geometries employing non-standard geometries and cusped magnetic fields. Hence, it was necessary to develop a replacement Hall thruster code. In this paper, we report on the development. We also summarize governing equations, and present preliminary results from the self-consistent mobility calculation.

*Contact email: lubos.brieda@particleincell.com
†Professor, Department of Mechanical and Aerospace Engineering

II. Hall thruster model

The new HET solver was developed within Starfish [4]. Starfish is a two-dimensional (Cartesian or axisymmetric) code for fluid dynamics, gas kinetics, and plasma physics. It has been used for a wide range of problems, including modeling infiltration and removal of molecular contaminants from a purged cavity [5], computation of conductance across a labyrinth vent [6], and analyzing the impact of surface roughness on secondary electron emission [7].

A. Electron Current

We have previously attempted to model Hall thrusters with Starfish using the thermalized potential approach. That effort was not fruitful, as the solver had difficulties with the cylindrical Hall thruster geometry being studied. New solver was thus developed following the two-dimensional formulation of Geng [8]. Electron momentum equation can be written as

$$\vec{j_e} = \mu\left(\vec{j_e} \times \vec{B}\right) + \sigma\vec{E} + \frac{\sigma}{en_e}\nabla p_e \tag{1}$$

where $\vec{j_e}$ is the electron current, p_e is the electron pressure, $\vec{B}$ is the magnetic field, $\sigma = \mu n_e e$ is the conductivity, m_e is the electron mass, and μ is the mobility. Using the equation of state (ideal gas, $p = nkT^K \equiv neT$), the pressure gradient is rewritten as $\nabla p_e = en_e\nabla T_e + eT_e\nabla n_e$. Here T_e is the electron temperature in eV units. With this substitution, electron current density is given by the following generalized Ohm's Law formulation:

$$\vec{j_e} = \mu(\vec{j_e} \times \vec{B}) + \sigma\vec{E} + \sigma(\nabla T_e + T_e\nabla \ln n) \tag{2}$$

Expanding the Hall term, a set of three equations can be obtained for components in the axial, radial, and azimuthal directions:

$$j_z = \mu(j_r B_\theta - j_\theta B_r) + \sigma E_z + \sigma(\nabla_z T_e + T_e\nabla_z \ln n) \tag{3}$$
$$j_r = \mu(j_\theta B_z - j_z B_\theta) + \sigma E_r + \sigma(\nabla_r T_e + T_e\nabla_r \ln n) \tag{4}$$
$$j_\theta = \mu(j_z B_r - j_r B_z) + \sigma E_\sigma + \sigma(\nabla_\theta T_e + T_e\nabla_\theta \ln n) \tag{5}$$

Due to axisymmetric geometry of the HT, the electric field and gradients of electron temperature and density are assumed to be zero in the azimuthal direction. It should be noted that this is a simplification in light of recent experiments demonstrating azimuthal spokes [9]. The azimuthal current density then reduces to $j_\theta = \mu(j_z B_r - j_r B_z)$ and can be substituted into Eqs. 3 and 4. This leads to the following set of coupled linear equations:

$$j_z = \mu\left[j_r B_\theta - \mu(j_z B_r - j_r B_z)B_r\right] + \sigma E_z + \sigma(\nabla_z T_e + T_e\nabla_z \ln n) \tag{6}$$
$$j_r = \mu\left[\mu(j_z B_r - j_r B_z)B_z - j_z B_\theta\right] + \sigma E_r + \sigma(\nabla_r T_e + T_e\nabla_r \ln n) \tag{7}$$

This system can be solved by matrix inversion to isolate the axial and radial component of the electron current density,

$$j_z = \mu_{11}\sigma(E_z + \nabla_z T_e + T_e\nabla_z \ln n) + \mu_{12}\sigma(E_r + \nabla_r T_e + T_e\nabla_r \ln n) \tag{8}$$
$$j_r = \mu_{21}\sigma(E_z + \nabla_z T_e + T_e\nabla_z \ln) + \mu_{22}\sigma(E_r + \nabla_r T_e + T_e\nabla_r \ln n) \tag{9}$$

where

$$\mu_{11} = \frac{1 + \mu^2 B_z^2}{1 + \mu^2 B^2}$$

$$\mu_{12} = \frac{\mu B_\theta + \mu^2 B_z B_r}{1 + \mu^2 B^2}$$

$$\mu_{21} = \frac{-\mu B_\theta + \mu^2 B_z B_r}{1 + \mu^2 B^2}$$

$$\mu_{22} = \frac{1 + \mu^2 B_r^2}{1 + \mu^2 B^2}$$

B. Mobility Models

The analytical mobility model used for comparison with kinetic results was composed of two terms: classical elastic scattering from heavy particles (n), and Bohm diffusion (b):

$$\nu_n = n_n \sigma_{e,n} v_{e,th} \tag{10}$$
$$\nu_b = 16\omega_c \tag{11}$$
$$\tag{12}$$

where $\omega_c = eB/m_e$. Here $\sigma_{e,n}$ is the electron-neutral momentum transfer cross-section. To allow for sensitivity studies, we introduce scaling coefficients and define cross-field mobility as

$$\mu_\perp = \alpha_n \frac{\mu_0}{1 + (\omega_c/\nu_n)^2} + \alpha_b \frac{e}{m\nu_b} \tag{13}$$

where $\mu_0 = e/(m_e\nu_n)$.

C. Potential Solver

Defining $j = j_e - j_i$, total current density can be written as

$$j_z = Z_1 E_z + Z_2 E_r + Z_3 \tag{14}$$
$$j_r = R_1 E_z + R_2 E_r + R_3 \tag{15}$$

where

$$Z_1 = \mu_{11}\sigma \tag{16}$$
$$Z_2 = \mu_{12}\sigma \tag{17}$$
$$Z_3 = \mu_{11}\sigma\left(\nabla_z T_e + T_e \nabla_z \ln n\right) + \mu_{12}\sigma\left(\nabla_r T_e + T_e \nabla_r \ln n\right) - e n_i u_{i,z} \tag{18}$$
$$R_1 = \mu_{21}\sigma \tag{19}$$
$$R_2 = \mu_{22}\sigma \tag{20}$$
$$R_3 = \mu_{21}\sigma\left(\nabla_z T_e + T_e \nabla_z \ln n\right) + \mu_{22}\sigma\left(\nabla_r T_e + T_e \nabla_r \ln n\right) - e n_i u_{i,r} \tag{21}$$

Then using current conservation

$$\frac{\partial j}{\partial z} + \frac{\partial j}{\partial r} + \frac{j_r}{r} = 0 \tag{22}$$

we can obtain

$$\left[Z_1^n E_z^n - Z_1^s E_z^s\right]\Delta r + \left[R_2^e E_r^e - R_2^w E_r^w\right]\Delta z = -S \tag{23}$$

where

$$S = \left[(Z_2^e E_r^e + Z_3^e) - (Z_2^w E_r^w + Z_3^w)\right]\Delta r + \left[(R_1^n E_z^n + R_3^n) - (R_1^s E_z^s + R_3^s)\right]\Delta z + \frac{1}{r}\left[R_1 E_z + R_2 E_r + R_3\right]\Delta z \Delta r \tag{24}$$

and n, s, e, and w are the values at the north, south, east, or west boundary of the node. Next, utilizing the electrostatic assumption allows us to write $\vec{E} = -\nabla\phi$. Then using the standard finite difference formulation, Equation 23 can be rewritten as

$$\phi_{i,j} = \left[\frac{1}{(Z_1^e + Z_1^w)\Delta^2 r + (R_2^n + R_2^s)\Delta^2 z}\right] \tag{25}$$
$$\left[(Z_1^e \phi_{i+1,j} + Z_1^w \phi_{i-1,j})\Delta^2 r + (R_2^n \phi_{i,j+1} + R_2^s \phi_{i,j-1})\Delta^2 z + S\Delta z \Delta r\right] \tag{26}$$

D. Boundary Conditions

Boundary conditions need to be applied at four distinct regions: along thruster walls, the axis of symmetry, the anode, and the cathode. Along the walls, zero electric field was applied in the normal direction, $\partial\phi/\partial n = 0$. At the axis of symmetry, we have $\partial\phi/\partial r = 0$. Dirichlet boundary $\phi_{anode} = 300$V was applied at the anode. We investigated setting a fixed potential along a prescribed cathode line, similar to HPHall, but found this have only a minimal impact on the potential in the channel. As such, results presented here were computed with $\phi = 0$ set on the downstream boundary. Zero electric field in the surface normal direction was set along thruster walls. Magnetic field lines were constructed from the stream function λ,

$$\frac{\partial\lambda}{\partial z} = rB_r$$
$$\frac{\partial\lambda}{\partial r} = -rB_z$$

E. Electron Temperature

In this report, electron temperature profile was set to experimental data presented in [10]. Magnetic field lines were assumed to be isothermal. Development of a self-consistent temperature solver is left for future work.

F. Ion Current

Neutrals and ions were modeled using the ES-PIC method. Neutrals were injected at the anode. The ionization model described below was used to generate ions. Particle positions were advanced forward in time from $\partial\vec{x}/\partial t = \vec{v}$ and for the case of ions, $\partial\vec{v}/\partial t = (q/m)\vec{E}$. The electric field was obtained by differentiating the potential, $\vec{E} = -\nabla\phi$. Ion current was computed from $\vec{j}_i = en_i\vec{u}_i$, where n_i and $\vec{u}_i$ are interpolations of particle data to the computational mesh.

G. Ionization Modeling

First-degree ionization was modeled as $\dot{n}_i = k(\theta)n_a n_e$, where the ionization rate is computed using the model of Fife as

$$k(\theta) = Q\beta_1 \frac{I(\theta)}{\theta^{3/2}} \tag{27}$$

where $\theta = kT_e/\epsilon_i$, $u = \epsilon/\epsilon_i$, $Q = 4.13 \times 10^{-13}$ m^3/s, $\beta_1 = 1.00$, $\beta_2 = 0.80$ (for Xenon), and

$$I(\theta) = \int_1^\infty e^{-\frac{u}{\theta}} \frac{(u-1)}{u} \ln(1.25\beta_2 u) du \tag{28}$$

Creation of doubly-charged Xe^{++} ions was not considered in this work.

III. Kinetic Mobility Model

Just like Starfish, the kinetic electron transport code Lynx also implements the PIC method. Only electrons are modeled kinetically, since the heavy particles can be assumed to remain frozen in the timespan required to compute cross-field transport. As noted earlier, the simulation input is a magnetic field lambda mesh containing multiple radial grid lines, each corresponding to an individual magnetic field line. Since electrons are magnetized, computation for each grid line can be computed independently. The simulation thus begins by the code initializing an independent one-dimensional simulation for each field line. These simulations are launched as threads, allowing multiple simulations to run in parallel. The number of concurrent runs is governed by number of available cores. As runs finish, new threads are launched from the pool until all field lines are processed. Upon completing, data is interpolated onto the lambda mesh. The vertical spacing of the lambda mesh does not have any impact on the kinetic simulations. It only controls the resolution of mobility in the Starfish simulation.

A. Particle Loading

The computational domain for each simulation is the single magnetic field line. The domain is discretized into number of cells, with the mesh spacing selected as a fraction of the Debye length. Typically, $\Delta h = 0.5\lambda_D$ is used. The simulation then continues by loading electrons according to ion density. The number of simulation macroparticles per cell is governed by a user parameter, which was set to 200 for this study. Typical simulation consisted of 100 mesh cells and 20,000 particles. Initial velocities are set by sampling the Maxwellian distribution function at the field line electron temperature. As noted by Fox [11], variable macroparticle weight is beneficial for resolving the high energy tail of the velocity distribution function. We did not take this approach at this time, but plan to incorporate it in the future. Electrons were loaded with guiding center at $z = 0$. The time step Δt was selected such that electrons completed a single orbit in 75 time steps.

Electron velocities were updated by integrating $\partial\vec{v}/\partial t = -(e/m_e)(\vec{E}+\vec{v}\times\vec{B})$ using the Boris method. The electric field consists of two components, $E_{\|}$ and $E_{\perp}$. The tangential contribution was obtained by solving Poisson's equation $\partial\phi/\partial s = -e(n_i - n_e)/\epsilon_0$. Here s is the distance along the field line. The boundary conditions were set from Gauss' law $\int_V \nabla \cdot \vec{E} ds dA = Q/\epsilon_0$ which allowed us to include surface charge collected on the dielectric walls. The normal component of the electric field was a simulation input, and relates to the potential drop across the thruster discharge channel. The initial electron density was loaded such that $n_e = n_i$ everywhere. This relationship is not valid in the sheath. We allowed the code to compute the sheath drop self-consistently. In the first phase of the simulation, scattering processes such as collisions and secondary electron emission was not enabled. Electrons impacting the wall were removed. This phase continued until potential drop was established with zero net flux to the walls, $\Gamma_E \approx \Gamma_i$. Since ions were not modeled as particles, the ion flux was estimated from $n_i v_0$, where v_0 is the Bohm velocity. Additional detail are outlined in [12].

B. Collisions and Near Wall Conductivity

Electrons were then reloaded using the macroparticle count corresponding the sheath solution. This reloading allowed us to repopulate the velocity distribution function, since the high energy particles are preferentially lost to the walls during the first phase. Simulation then continued with phase two in which collisions and secondary electron emission were considered. Mobility calculations were also performed. Any particles found to scatter sufficiently far away from the field line were removed and replaced with new particles sampled from the Maxwellian.

Electron collisions were modeled using the Monte Carlo method. In this method, source particles are collided with a stationary target cloud. The collision probability is determined from the background density, n_0 and collision frequency is $P = 1 - \exp(-n_0\sigma_0 g\Delta t)$. Here σ_0 is the total collision cross-section due to all processes. The collision process was picked randomly according to the ratio of σ_i/σ_0. Post-collision velocity was computed by first sampling a random target velocity and a random impact angle. We then calculated the post-collision velocity from conservation of energy. To reduce statistical errors and improve performance, collisions were computed only once every 4 timesteps. Five types of collisions were considered: momentum-transfer (electron-atom), ionization (electron-atom), excitation (electron-atom), and Coulomb (electron-electron and electron-ion). Momentum transfer, ionization, and excitation cross-sections were computed using the polynomial fits given by Szabo [13]. The inelastic collisions were modeled by reducing the energy of the impacting electron by the ionization or excitation energy, and scattering the electron through a random angle. Electrons impacting the dielectric walls were reflected back to the domain, absorbed, or generated secondary electrons according to the model of Dunaevsky [14]. The secondary electron yield was given by

$$\gamma = \left(\frac{E_p}{35\text{eV}}\right)^{0.5} \tag{29}$$

The SEE electrons were assumed to leave the surface unmagnetized, and were generated at the wall with initial direction given by the cosine distribution. Impacting electrons were absorbed by the wall.

C. Transport Calculation

Mobility relates the cross-field drift speed and the electric field, $v_{\perp} = \mu_{\perp} E_{\perp}$. Computing mobility thus requires estimating $v_{\perp}$ at nodes of the simulation domain, and dividing by the local electric field. There

are two ways to determine this speed: by averaging the z component of velocity, or from guiding center drift. Both methods were implemented and were found to be in a good agreement. The guiding center approach evaluates the center once per per orbit as $r_g = 0.5(z^+ + z^-)$, where z^+ and z^- are the extents of particle's position. Drift velocity is then $v_\perp = r_g/t$ where t is the time delta since previous sampling. Only particles that have diffused more than r_L were counted. The local Larmor radius r_L was computed using particle's tangential velocity, and the strength of the magnetic field at the particle location. Particles diffusing sufficiently far from the field line were removed from the simulation and subsequently replaced by new particles centered on the field line. The tangential position of the new particles was based on the ion density.

D. Starfish/Lynx Coupling

Both Lynx and Starfish were developed in Java. Interfacing the two codes was easily accomplished by importing Lynx as a library into Starfish and writing a wrapper for interpolating results from the Starfish domain onto the lambda mesh used by Lynx. Subset of the code is shown below. Since Lynx was initially developed to read the inputs from a file, the data handling is performed by a class called Reader. The RunSims method implements the thread pool. After Lynx completes, Starfish uses the analytical model to compute mobility everywhere. The lambdaToDomain method then interpolates Lynx mobility unto the nodes of the Starfish computational mesh. Nodes outside the lambda mesh are not affected, and hence retain mobility from the analytical model.

```
/*interpolate data from r-z to lambda mesh*/
lambda_mesh.domainToLambda();

/*generate Lynx data structures using Starfish data*/
lynx.Reader reader = new lynx.Reader(lambda_mesh.ni,lambda_mesh.nj,Z,R,
                     LAMBDA,BF,NA,NE,UPERP,EPERP,TE);

/*launch simulations, multiple field lines processed in parallel*/
lynx.Main.RunSims(reader,settings);

/*compute mobility from analytical model*/
computeMobilityNB();

/*interpolate mobility from lambda mesh on overlapped nodes*/
lambda_mesh.lambdaToDomain();
```

IV. Simulation Setup and Results

A. Simulation Domain

Testing was performed using the PPPL cylindrical Hall thruster (CHT) [15] configuration studied previously. This thruster consists of an annular zone leading to a cylindrical section. The inner radius of the cylindrical section is approximately 1.5cm. Figure 1 shows the computational domain. The green and blue markers are the nodes of the computational mesh used by Starfish to compute the potential per Equation 26. Potential was solved only on the blue (fluid) nodes. The purple mesh spanning most of the annular section and portion of the cylindrical section is the lambda mesh used by Lynx for mobility calculation. The vertical (constant i) grids follow the magnetic field lines. Contours of the magnetic field strength are shown in black. Finally, the red lines indicate the geometry boundaries. Initially, we anticipated modeling the entire bounded region. However, due to lack of magnetic field data, the computational domain was reduced as shown.

B. Initial Results with Analytical Mobility

Figure 2 shows results obtained using the 2D potential solver after 6000 time steps at 1×10^{-8} s. As mentioned earlier, our code does not yet contain a temperature solver. Figure 2(b) plots the electron temperature, which was an input and did not change during the simulation. This is a significant inconsistency in our code that

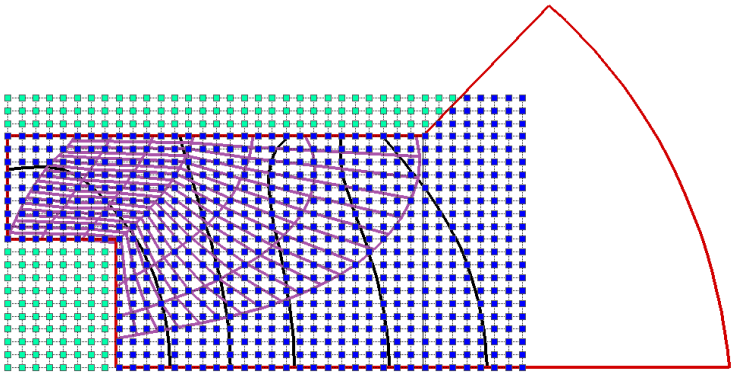

Figure 1. Simulation domain. The green markers indicate nodes outside the fluid domain. The lambda mesh used by Lynx to compute mobility is shown in purple. Magnetic field contours are shown in black.

will be addressed in the future by developing a temperature solver. Therefore, the potential profile shown here should not be considered a valid solution for this thruster. Yet, the solution is sufficient for testing kinetic mobility calculation. Ion density is proportional to the neutral density and electron temperature.

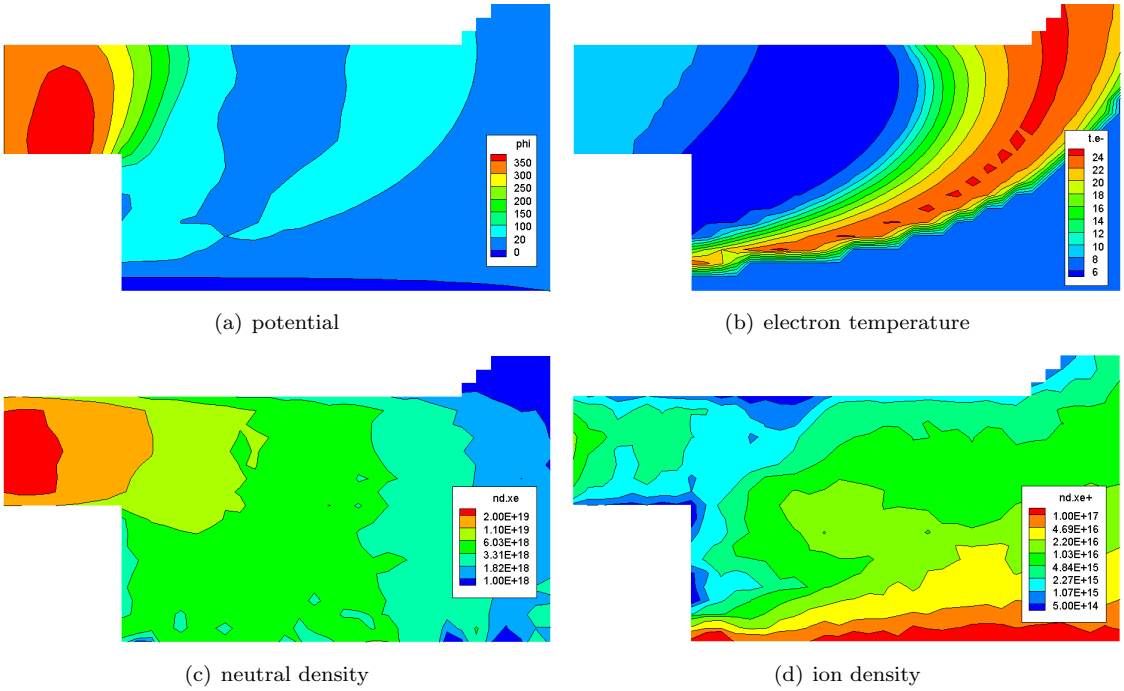

(a) potential

(b) electron temperature

(c) neutral density

(d) ion density

Figure 2. Preliminary results from the two-dimensional potential solver. Temperature profile was set to experimental data and did not change during the simulation.

Figures 3(a) and 3(b) plot mobility from the analytical model in Equation 13. Since Bohm mobility is only a function of the magnetic field, it does not change with time. The classical mobility is based on electron-neutral collisions and as such varies according to the evolution of the neutral density as well as temperature. The plot shown here illustrates the typical values corresponding to the system in Figure 2. The objective of our integration study was to determine how similar (or different) the results from the kinetic model will be to the values in Figure 3.

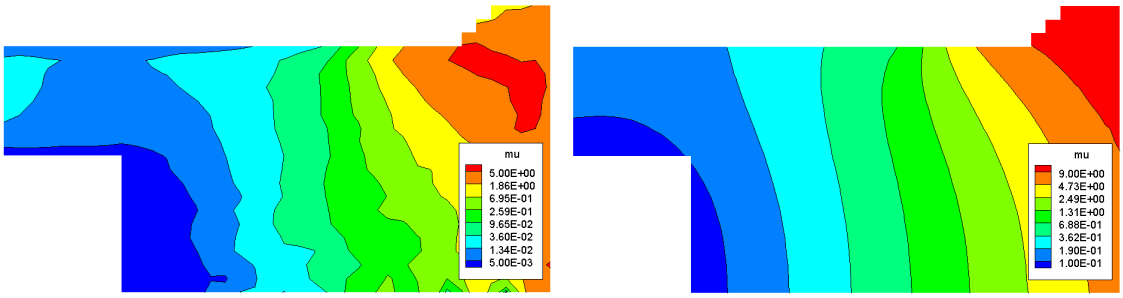

(a) $\mu_{\perp,n}$ (b) $0.15\mu_B$

Figure 3. Contributions to the analytical mobility model.

C. Kinetic Simulation

Figure 4 shows potential and electron densities along a single magnetic field line. This is one of many outputs of Lynx. The code generates a large set of diagnostic data, including transport parameters, particle traces, and cross and parallel velocity distribution functions. The red line plots the ion density coming from the Starfish simulation. Since ions are not modeled as particles, it is this distribution that is used when adding the n_i term to the Poisson's equation. The blue curve is the electron density. The small oscillations correspond to the statistical noise typical of kinetic simulations. Important is noticing that the two curves follow each other in the bulk plasma. Near the walls, electron density is lower than the ion density as predicted by the sheath theory. Similarly, potential is approximately uniform in the bulk but decays rapidly near the walls. The sheath potential drop is within few times the electron temperature, as expected.

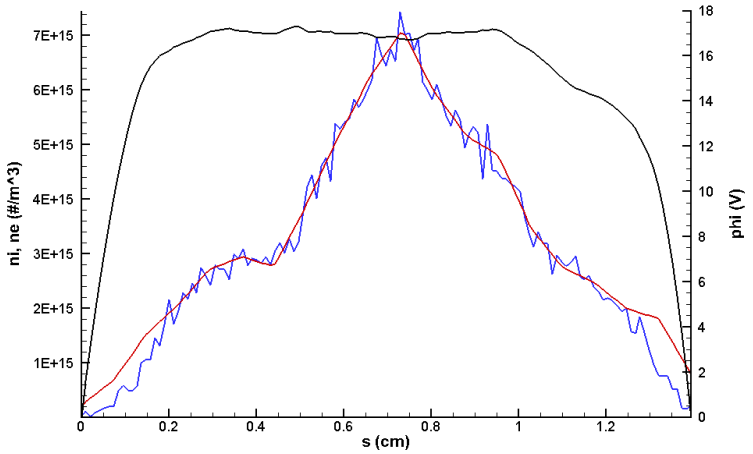

Figure 4. Typical ion (red), electron (blue) densities and potential (black) along a magnetic field line. Sheath drop can be seen in both potential and electron density.

Figure 5 shows trace of a secondary electron emitted at the outer wall. Both figures show the same data from a different perspective. The color indicates time, with blue being older than red. The particle can be seen orbiting about the field line, with the Larmor radius constricting as the particle moves to the region of stronger field. The particle eventually reflects, either due to the electric field or the $\partial B/\partial s$ gradient. It spirals back towards the outer wall. Here it most likely impacts the wall and is re-emitted as a new secondary. The jump due to this re-emission is the fundamental idea behind near wall conductivity. The particle then continues towards the inner wall, reflects back, and the process repeats. The top-down view shown in Figure 5(b) further illustrates this walk. Because of the axisymmetric domain, Lynx considers only the z (horizontal) motion when computing mobility. These shifts in the guiding center are used to compute the local drift speed.

The aggregate of individual particle drifts, either due to wall-effects or heavy particle collisions, allows us to compute the cross-field electron current. The result for two magnetic field lines is shown in Figure

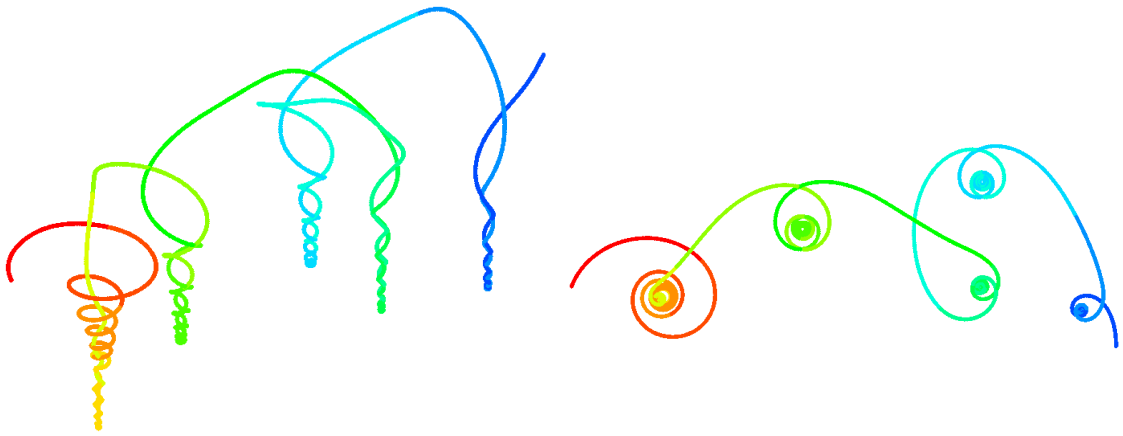

(a) side view (b) top view

Figure 5. Trace of a secondary electron oscillating between two walls with increasing magnetic field strength towards the inner wall.

6. The data was normalized by the field line length and the current magnitude to bring both sets of data onto same axis. Oscillatory current density typical of near wall conductivity is clearly seen, especially for the most downstream field line. Model for this oscillatory current density was described by Keidar [16]. Similar current densities were reported on earlier in an experimental and numerical work of Yu [17]. We also obtained similar results in a previous hydrodynamic study [18].

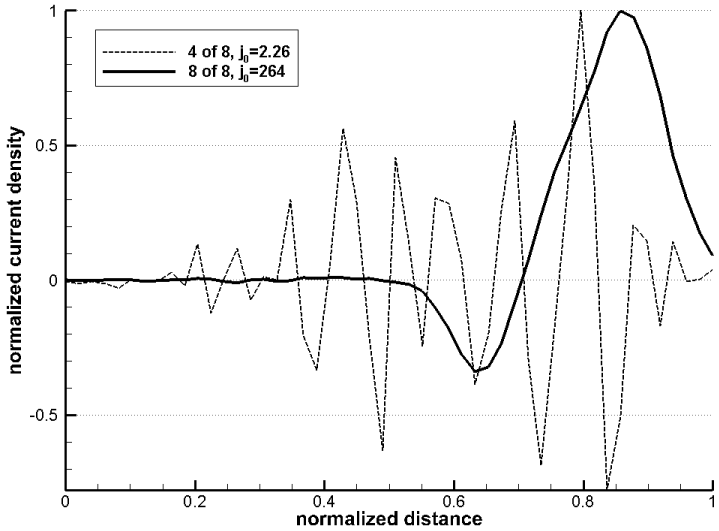

Figure 6. Normalized current density for two magnetic field lines. Oscillatory pattern characteristic of NWC can be seen.

D. Lynx Mobility

Combining mobilities obtained along each field line results in the profile shown in Figure 7(a). The values outside the lambda mesh came from the analytical model. As can be seen, the two sets are in a good agreement. Although the profiles differ, the magnitudes of mobility obtained from the kinetic simulation are comparable to the magnitudes from the analytical model. To investigate the relationship further, we proceeded to compute the difference between this kinetic result, μ_L, and the analytical model. Figure 7(b) shows the deviation from the classical collisional mobility, μ_n. We can see that in the center of the annular channel, the two results agree surprisingly well, with the difference limited to under 5×10^{-2} m^2/Vs. In

Figures 7(c) and 7(d) we perform a similar subtraction but consider only the Bohm diffusion. The first of these two images shows the subtraction with Bohm coefficient 0.15, as used in the study. The second figure shows the subtraction with this coefficient set to 1.

By subtracting both classical and Bohm diffusion, we obtain the plot in Figure 7(e). Now, since the results are plotted on a log scale, it's not possible to visualize negative values directly. As such, Figure 7(f) shows the inverse of this subtraction. Studying these two plots we notice fascinating trends in the results. The kinetic and analytical mobilities are similar, but the kinetic model predicts slightly lower mobility in the center of the annular channel. On the other hand, it predicts increased mobility near the walls. This seems to indicate that near wall conductivity is an important player in this thruster. We also obtain significantly higher mobility near the outer wall close to the thruster exit. Such an increase is predicted by the analytical model (see Figure 3), however the kinetic code predicts almost two orders of magnitude higher values.

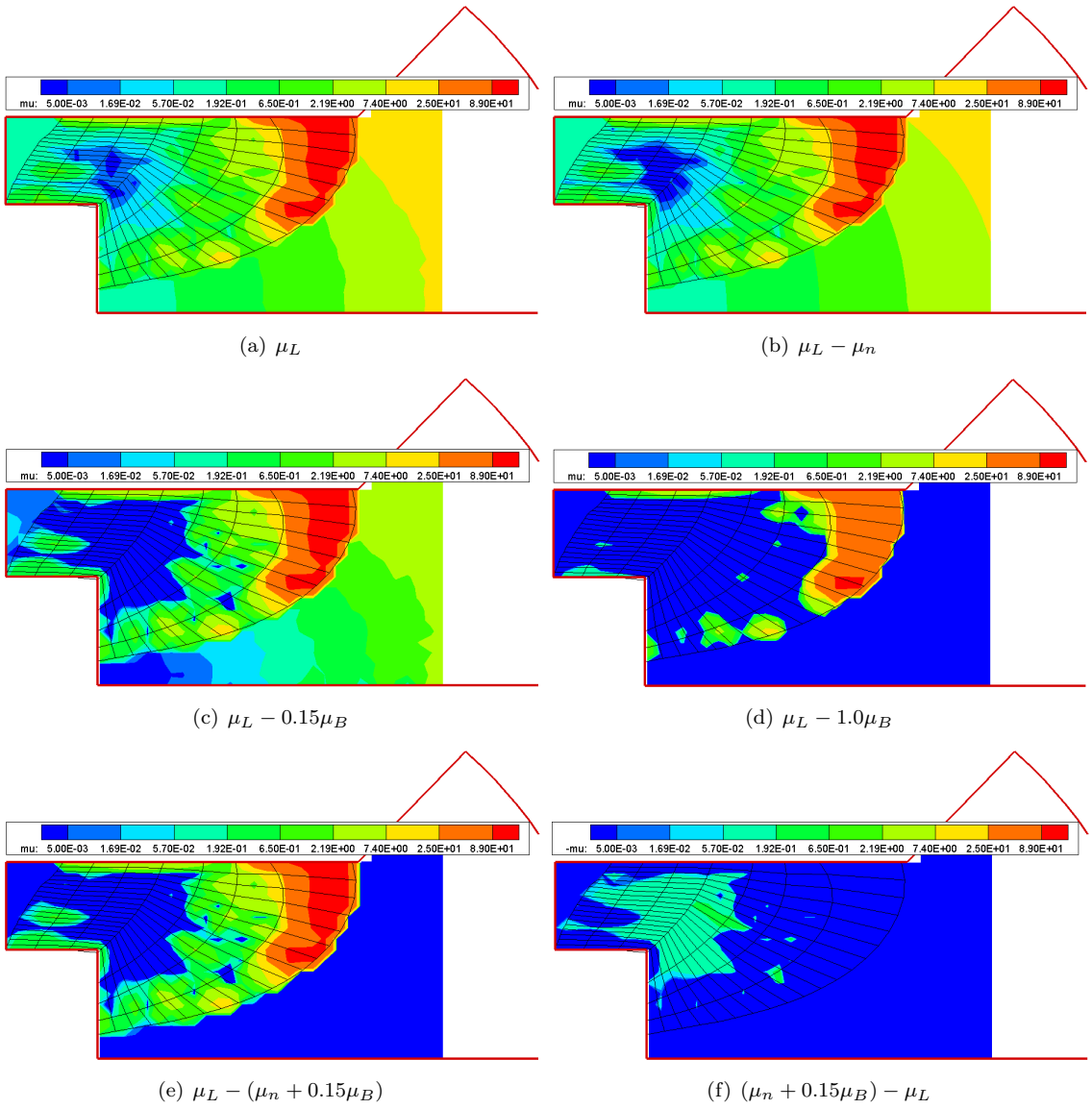

(a) μ_L (b) $\mu_L - \mu_n$

(c) $\mu_L - 0.15\mu_B$ (d) $\mu_L - 1.0\mu_B$

(e) $\mu_L - (\mu_n + 0.15\mu_B)$ (f) $(\mu_n + 0.15\mu_B) - \mu_L$

Figure 7. (a) shows mobility computed by Lynx with the areas outside the lambda mesh computed from the analytical model. The remaining plots show the difference between the Lynx mobility μ_L and various components of the analytical model.

.

E. Thruster Simulation with Kinetic Mobility

Finally, to demonstrate the feasibility of running a Hall thruster simulation with the kinetically determined mobility, we continued the simulation in Figure 2 for five additional time steps. During these five steps, mobility was computed as shown above. Potential and ion density profiles from this run are in Figure 8. Difference in the potential solution can be seen. However, until a self-consistent temperature solver is implemented, it won't be possible to characterize the impact of the kinetic model on the predictive capability of the simulation.

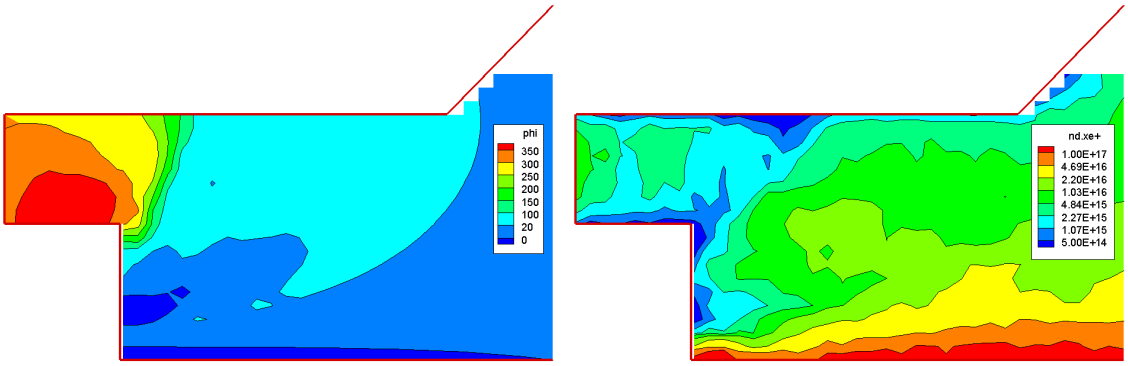

(a) potential (b) ion density

Figure 8. Results after five additional iterations with the Lynx computed mobility.

V. Summary and Future Work

In this paper we developed formulation for a two-dimensional potential solver for Hall thrusters. We also demonstrated a promising coupling with a kinetic code to compute mobilities in the thruster self-consistently. The kinetic approach resulted in mobility values in good agreement with the analytical model. At the same time, it predicted higher near-wall transport, as well as higher mobility in the region near the thruster exit. Mobilities shown here were obtained after 10,000 electron time steps. The wall time to compute each field line was about 2 minutes on a Lenovo i7 2.4 GHz laptop. Since our domain consisted of eight field lines, but only seven were run at once, the total computational time was about 4 minutes. This is not a particularly long time, however, expending such an effort at every time step of the thruster simulation is clearly not numerically feasible. Typical Hall thruster simulations run for hundreds of thousands time steps. As such, we propose to use the kinetic code to compute deviation from the analytical model and use it as a third term in the overall mobility, $\mu_\perp = \alpha_n\mu_n + \alpha_b\mu_b + \alpha_L\mu_L$. This term would be updated periodically at some user-specified frequency (such as every 100 time steps), or could be updated automatically based on spatial or temporal gradients (such as when ion density or electron temperature changed more than some tolerance). In addition, our Hall thruster code needs to be extended to include a temperature solver. These two items are planned to be addressed as part of future work.

Acknowledgment

Funding for the initial Starfish / Lynx coupling investigation was provided by NASA SBIR contract NNX12CD98P.

References

[1]Brieda, L. and Keidar, M., "Multiscale Modeling of Hall Thrusters," *32nd International Electric Propulsion Conference*, Wiesbaden, Germany, 2011.

[2]Morozov, A. I. and Savel'ev, V., "Theory of the Near-Wall Conductivity," *Plasma Physics Report*, Vol. 27, No. 7, 2001.

[3]Fife, J. M., *Two-Dimensional Hybrid Particle-In-Cell Modeling of Hall Thrusters*, Master's thesis, Massachusetts Institute of Technology, 1998.

[4]Brieda, L. and Keidar, M., "Development of the Starfish Plasma Simulation Code and Update on Multiscale Modeling

of Hall Thrusters," *48th AIAA Joint Propulsion Conference*, Atlanta, GA, 2012.

[5]Brieda, L., Newcome, J., and Errigo, T., "Diffusion of Water into Purged Volumes," *SPIE Optics & Photonics Conference*, San Diego, CA, 2014.

[6]Brieda, L. and Gordon, T., "Analysis of molecular conductance through a labyrinth vent," *SPIE Optics & Photonics Conference*, San Diego, CA, 2014.

[7]Rose, L. P., *Development of 1D Particle-in-Cell Code and Simulation of Plasma-Wall Interactions*, Master's thesis, George Washington University, 2014.

[8]Geng, J., Brieda, L., and Michael, K., "On applicability of the "thermalized potential" solver in simulations of the plasma flow in Hall thrusters," *Journal of Applied Physics*, Vol. 114, No. 103305, 2013.

[9]Ellison, C., Raitses, Y., and Fisch, N., "Cross-field electron transport induced by a rotating spoke in a cylindrical Hall thruster," *Physics of Plasmas*, Vol. 19, No. 1, 2012, pp. 013503.

[10]Raitses, Y., Smirnov, A., and Fisch, N. J., "Effects of enhanced cathode electron emission on Hall thruster operation," *Physics of Plasmas*, Vol. 16, No. 05716, 2009.

[11]Fox, J., *Advances in Fully-Kinetic PIC Simulations of a Near-Vacuum Hall Thruster and Other Plasma Systems*, Ph.D. thesis, Massachusetts Institute of Technology, 2007.

[12]Brieda, L., *Multiscale Modeling of Hall Thrusters*, Ph.D. thesis, The George Washington University, 2012.

[13]Szabo, J., *Fully Kinetic Numerical Modeling of a Plasma Thruster*, Ph.D. thesis, Massachusetts Institute of Technology, 2001.

[14]Dunaevsky, A., Raitses, Y., and Fisch, N., "Secondary electron emission from dielectric materials of a Hall thruster with segmented electrodes," *Physics of Plasmas*, Vol. 10, 2003, pp. 2574.

[15]Raitses, Y. and Fisch, N. J., "Parametric investigations of a nonconventional Hall thruster," *Physics of Plasmas*, Vol. 8, No. 05, 2001.

[16]Keidar, M. and Beilis, I. I., "Electron Transport Phenomena in Plasma Devices With $E \times B$ Drift," *IEEE Transactions on Plasma Science*, Vol. 34, No. 3, 2006.

[17]Yu, D., Wu, Z., and Wang, X., "Numerical simulation for near wall conductivity effect on current profiles in the annular channel of Hall-type stationary plasma thrusters," *Physics of Plasmas*, Vol. 12, No. 043507, 2005.

[18]Keidar, M. and Brieda, L., "Modeling electron transport within the framework of hydrodynamic description of Hall thrusters," *44th AIAA Joint Propulsion Conference*, Hartford, CT, 2008, AIAA-2008-5186.